

## Dual-acquisition phase-sensitive fat–water separation using balanced steady-state free precession

Brian A. Hargreaves<sup>a,\*</sup>, Neal K. Bangerter<sup>b</sup>, Ann Shimakawa<sup>c</sup>, Shreyas S. Vasanawala<sup>a</sup>,  
Jean H. Brittain<sup>c,d</sup>, Dwight G. Nishimura<sup>b</sup>

<sup>a</sup>Department of Radiology, Stanford University, Stanford, CA 94305-5488, USA

<sup>b</sup>Magnetic Resonance Systems Research Laboratory, Department of Electrical Engineering, Stanford University, Stanford, CA 94305-5488, USA

<sup>c</sup>Applied Science Lab West–General Electric Health Care, Menlo Park, CA, USA

<sup>d</sup>Global Applied Science Laboratory, GE Healthcare, Madison, WI, USA

Received 4 August 2005; accepted 22 October 2005

### Abstract

Balanced steady-state free precession (SSFP) sequences use fully refocused gradient waveforms to achieve a high signal and useful image contrast in short scan times. Despite these strengths, the clinical feasibility of balanced SSFP is still limited both by bright fat signal and by the signal voids that result from off-resonance effects such as field or susceptibility variations. A new method, dual-acquisition phase-sensitive SSFP, combines the signals from two standard balanced SSFP acquisitions to separate fat and water while simultaneously reducing the signal voids. The acquisitions are added in quadrature and then phase corrected using a simple algorithm before fat and water can be identified simply by the sign of the signal. This method is especially useful for applications at high field, where the RF power deposition, spatial resolution requirements and gradient strength limit the minimum repetition times. Finally, dual-acquisition phase-sensitive SSFP can be combined with other magnetization preparation schemes to produce specific image contrast in addition to separating fat and water signals. © 2006 Elsevier Inc. All rights reserved.

**Keywords:** Fat suppression; Rapid imaging; SSFP; Steady state

### 1. Introduction

Balanced steady-state free precession (SSFP) imaging sequences offer a relatively high signal and rapid 2D or 3D imaging, potentially overcoming two of the prime weaknesses of MRI [1–3]. However, the clinical applications of balanced SSFP are still limited by two main factors: First, the signal is very sensitive to resonant frequency variations that result from static field inhomogeneity, susceptibility variations or chemical shift [1,4]. Second, balanced SSFP produces a very bright signal from fat, which obscures visualization of other structures. Although much effort has been put forth to reduce these limitations, limited work to date has simultaneously addressed both [5], hence the motivation behind our study.

The sensitivity of the balanced SSFP to resonant frequency results in severe signal dropouts in regions of

high susceptibility variation or when the resonance frequency range after shimming is comparable with the inverse of the repetition time ( $TR$ ) [1,4,6–8]. Recent advances in gradient technology have resulted in  $TR$ s as short as 1–2 ms, allowing resonance frequency variations of 500–1000 Hz [9,10]. However, spatial resolution requirements as well as RF absorption (particularly at 3.0 T and higher) are more significant limitations on the minimum  $TR$ . Alternatively, the use of multiple acquisitions can synthesize a signal profile that is relatively smooth across a wide range of frequencies at the cost of increased number of acquisitions and some SNR efficiency [7,11–14].

The second major limitation of balanced SSFP in clinical applications is the bright fat signal that results from the  $T_2/T_1$  signal dependence of the sequence. Numerous techniques have been explored to separate fat and water in balanced SSFP. These can roughly be divided into three categories: transient fat saturation, steady-state fat suppression and steady-state fat–water separation.

Transient fat-suppression techniques are methods where fat is periodically suppressed, but the fat signal is tran-

\* Corresponding author. Lucas MRS Center, Stanford, CA 94305-5488, USA. Tel.: +1 650 498 5368; fax: +1 650 723 5795.

E-mail address: [bah@stanford.edu](mailto:bah@stanford.edu) (B.A. Hargreaves).

sient and slowly recovers during imaging. These include fat-saturated SSFP with cardiac gating [15] and with repeated fat-saturation pulses [16]. Although efficient, these techniques must be carefully implemented and can suffer from transient signals common in balanced SSFP [17].

The second category, steady-state fat suppression, refers to techniques that generate a steady state where fat produces a low signal and include fluctuating equilibrium MR [18], SLIMFEST [19], oscillating SSFP [20] and alternating- $TR$  balanced SSFP [21]. These methods do not suffer from transient effects but generally sacrifice some imaging efficiency of the sequence and can require very short  $TR$ s to achieve the desired profile or may require high RF linearity as in the cases of the studies discussed in References [19] and [20].

The final group, fat–water separation methods, acquires a high signal from both fat and water and separates the two signals in postprocessing. Such methods include linear-combination SSFP [13], SSFP using different Dixon techniques [22,23] and phase-sensitive SSFP [24]. The Dixon and linear-combination methods all require multiple acquisitions, whereas phase-sensitive SSFP is sensitive to partial-volume effects due to nonlinear separation. However, several recent works are attempting to solve this partial-volume problem [25–27], with encouraging results.

As is clear from the preceding paragraphs, there is already a wealth of methods that attempt to address the bright fat signal in balanced SSFP. In addition, there are numerous efforts in progress to improve on many of these techniques. A full comparison of techniques, which is beyond the scope of this article, must take into account SNR efficiency, number of acquisitions, partial-volume effects, robustness to static and RF field inhomogeneity, robustness to motion or flow, ability to perform partial acquisitions, reconstruction complexity and, ultimately, of course, the ability to work in a clinical setting.

We present a dual-acquisition phase-sensitive SSFP technique to separate fat and water while also mitigating the sharp signal nulls common in balanced SSFP at high resonant offsets. The only limitations of this technique are the partial-volume effects of phase-sensitive SSFP and the need for two acquisitions. However, the technique is otherwise very efficient and robust compared with most SSFP fat-reduction techniques. We show a description of the basis for dual-acquisition phase-sensitive SSFP, the details of the reconstruction and experimental results from the technique at 1.5 and 3.0 T.

## 2. Theory

In this section, we first review the characteristics of the balanced SSFP signal that are exploited in this technique and then outline a phase correction and separation process, which is similar to previous techniques for other MRI applications. The details of our phase correction are shown in Appendix A.

### 2.1. Signal characteristics

Balanced SSFP sequences consist of RF excitation pulses with flip angle  $\alpha$  and phase angle  $\phi$ . RF pulses are applied with a spacing of  $TR$ , and all slice-select and imaging gradients are fully rewound over a sequence repetition. After many repetitions, a steady state evolves, as is shown in Fig. 1 for echo time,  $TE = \frac{TR}{2}$ . In standard balanced SSFP sequences,  $\phi$  alternates between 0 and  $\pi$  on successive excitations, leading to the profile shown by the dashed line in Fig. 1, where spins that are on-resonance (0 Hz) produce a high signal. Alternatively, if  $\phi$  is held constant, then the dotted-line profile results [28]. In general, if the RF and acquisition phase  $\phi$  increase by  $\Delta\phi$  with each repetition, then signal nulls occur at resonant frequency offsets of  $\frac{k}{TR} + \frac{\Delta\phi}{2\pi TR}$ , where  $k$  is any integer. The signal phase at  $TE = \frac{TR}{2}$  is flat and alternates between  $\frac{\Delta\phi}{2} - \frac{\pi}{2}$  and  $\frac{\Delta\phi}{2} + \frac{\pi}{2}$ .

As shown by the solid line in Fig. 1, the sum of two acquisitions with a  $\Delta\phi$  of 0 and  $\pi$  gives a relatively flat magnitude profile [11,12] and a fairly linear phase profile. Intuitively, the profiles from the two acquisitions are similar to a cosine and a sine. Adding these in quadrature leads to a complex exponential (constant magnitude and linear phase). The amount of ripple in both the magnitude and phase will increase significantly as the flip angle decreases or as the  $T_2/T_1$  ratio increases, as described in the Discussion section [14].

### 2.2. Block-regional phase correction

In the sum of two signals (Fig. 1), a frequency shift of 210 Hz (or generally  $\frac{2\eta+1}{TR}$  where  $\eta$  is an integer) results in a

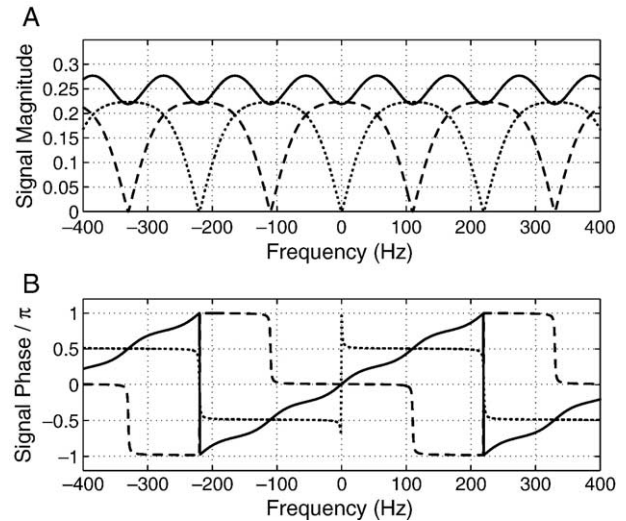


Fig. 1. The (A) magnitude and (B) phase of the signal in balanced SSFP at  $TE = TR/2$  for the standard case where the RF and demodulator phase increment by  $\pi$  on each excitation (dashed line) and for constant RF and demodulator phase (dotted line). If the complex signals from the two acquisitions are added, then the magnitude and phase of the resulting signal are shown by the solid lines. The magnitude of the sum is much flatter than that of the individual acquisitions, whereas the phase is fairly linear with resonant frequency. For this plot,  $T_1/T_2 = 900/200$  ms,  $TR/TE = 4.6/2.3$  ms and flip angle =  $60^\circ$ .

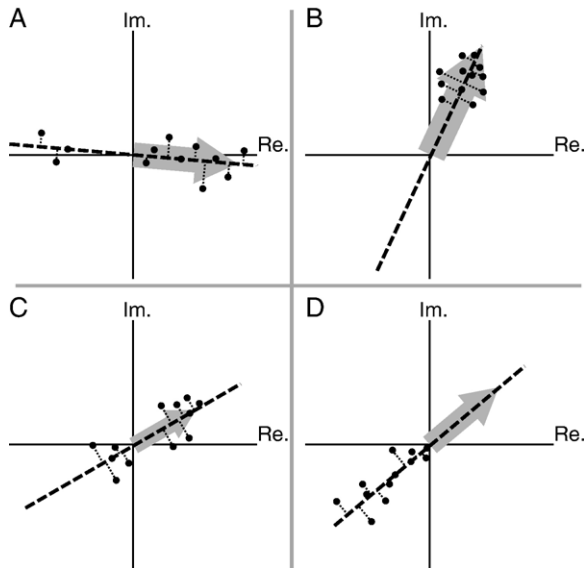


Fig. 2. Possible phase fit to four neighboring blocks in 2D. Initially, the dashed black line direction is determined for each block by minimizing the sum of the squared orthogonal distances (dotted lines) from the line to each pixel value in the complex plane. Panel (A) shows a block that contains a strong signal from both fat and water. Panel (B) shows a block containing only one tissue type. Panel (C) shows both tissue types but with a weaker signal. Panel (D) shows, assuming a slowly varying phase, the opposite tissue to Panel (B). The blocks are then traversed (e.g., in Order A–B–C–D), and the direction of the gray arrows is kept within  $90^\circ$  of the vector sum of the gray arrows from neighbor blocks. Finally, the phases in each block are rotated by the angle of the gray arrow to bring the gray arrow to the positive real axis. Full details of the fit are given in Appendix A.

phase difference of  $\pi$  radians, as with the individual acquisition. This difference can be used to separate fat and water voxels based on the chemical shift (at 1.5 T), provided that the phase variation due to other sources of off-resonance or image phase can be removed. We assume that the phase variation from other sources, including  $B_0$  inhomogeneity, susceptibility variations, coil sensitivity and slice profile phase, is slowly varying in space. We then use the following block-regional phase correction to remove

the slowly varying phase without affecting the phase shift due to chemical shift. This algorithm is very similar to the algorithms recently proposed by Ma [29] for phase-sensitive inversion recovery imaging and by Moriguchi et al. [30] for Dixon fat–water separation.

The following steps summarize the block-regional phase correction, with a diagram showing a 2D example shown in Fig. 2 and example images shown in Fig. 3 (algorithm details are given in Appendix A):

1. The reconstructed image [Fig. 3(A) and (B)] is divided into small blocks (e.g.,  $4 \times 4 \times 4$  pixels).
2. For each block, we assign the block phase as the angle of the best-fit line that passes through the origin and a scatter of all voxel values in the complex plane [dashed lines in Fig. 2 and phase shown in Fig. 3(C)].
3. Beginning with a selected block near the center of the image,  $\pi$  is added to each block phase as necessary to keep it consistent with the weighted sum of the block phases [Fig. 3(D)] of neighboring blocks. [Fig. 3(E) shows the resulting block phases.] Discontinuities of  $2\pi$  do not matter here.
4. The phase of each block is subtracted from the phase of all voxels within that block to leave the phase-corrected image [Fig. 3(F)].

At this point, the slowly varying phase has been removed and the voxel phases are closely aligned to either 0 or  $\pi$ . Selecting only voxels with a positive real part yields the water-only image, whereas selecting those with a negative real part gives the fat-only image. Displaying the magnitude of all pixels gives the same magnitude as the combined original image.

### 3. Methods

All scans at 1.5 T used a GE Signa Excite scanner (GE Health Care Technologies, Waukesha, WI, USA) and a linear transmit/receive extremity coil (Medical Advances, Milwaukee, WI, USA). Scans at 3.0 T used a GE Signa VH/i scanner

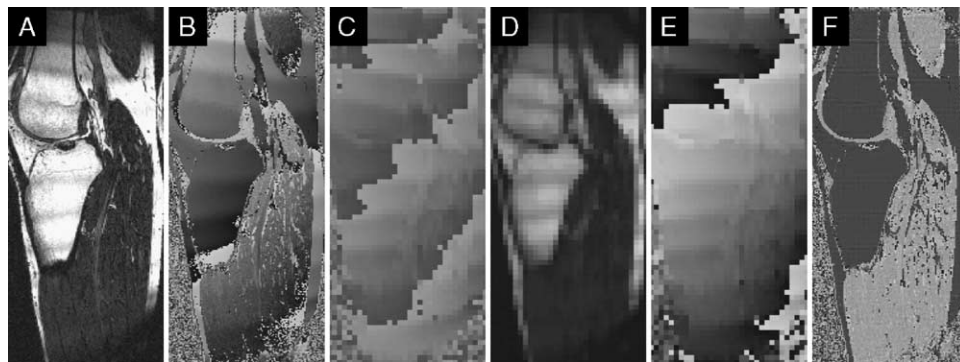


Fig. 3. Sample of phase-correction process. Panels (A) and (B) show the magnitude and phase of complex input signals. Panel (C) shows the angles of the best-fit line through the scatter for each block; Panel (D) shows the weights assigned to each block. Panel (E) shows the phase to remove after alignment. Panel (F) shows the corrected phase image. Notice that the phase removed [(E)] is slowly varying and that the final phase image has a sign change between fat and water voxels. Phase images are displayed with black–gray–white shades corresponding to increasing phase angles from  $-\pi$  to 0 to  $\pi$ .



with a quadrature transmit extremity coil (Medical Advances). Both scanners are equipped with CV/i gradients (40 mT/m maximum amplitude and 150 T/m/s maximum slew rate). Images were reconstructed offline using a simple Fourier reconstruction, followed by the block-regional phase correction described in the Theory section. Finally, fat and water images were obtained by selecting voxels with negative and positive real parts, respectively. The reconstruction and phase correction were implemented in Matlab 6.5 (Mathworks, Natick, MA, USA) — the phase-correction software is available at <http://www-mrsrl.stanford.edu/~brian/psssf/> both in Matlab and C.

### 3.1. Phantom validation

We first validated this technique using a simple bottle phantom filled with tap water and vegetable oil. Two 3D balanced SSFP images were acquired with a  $\Delta\phi$  of 0 and  $\pi$ . Other scan parameters were a  $30^\circ$  flip angle,  $TR/TE=4.6/2.3$  ms,  $320\times128\times128$  matrix and  $30\times12\times12.8\text{-cm}^3$  field of view (FOV). The readout was in the longer direction (30-cm FOV). In addition, a constant gradient of strength 0.1 mT/m was applied throughout scanning to create a resonant frequency variation of approximately 40 Hz/cm along the bottle. Susceptibility shifts from the air–phantom boundaries created additional resonant frequency shifts with rapid spatial variation. Image reconstruction, phase correction and voxel separation were performed using the method described above.

### 3.2. In vivo validation

The above mentioned protocol was repeated in the knee and lower leg of a healthy volunteer at 1.5 T. To validate the performance of the reconstruction, we repeated the scan with and without a constant gradient of 0.1 mT/m applied throughout the scan. Again, image reconstruction, phase correction and voxel separation were performed. Following separation, maximum intensity projection (MIP) images were also calculated to show the vasculature in the lower leg.

### 3.3. High-field application

At 3.0 T, it is difficult to obtain a shim where the frequency variation due to susceptibility or field inhomogeneity is less than  $1/TR$ , so our technique is very applicable. Assuming a chemical shift frequency difference of 420 Hz between fat and water, we selected  $TR=2TE=11.9$  ms or  $TR=5/(420\text{ Hz})$ . This places fat and water five signal bands apart. The longer  $TR$  increases scan time but allows improved imaging efficiency and spatial resolution while reducing the RF power deposition and potentially enables additional contrast mechanisms such as those described in Reference [31]. We scanned the legs of two healthy volunteers using a  $512\times240\times96$  matrix over a  $25\times17\times10\text{-cm}$  FOV and a  $45^\circ$  flip angle and performed the same reconstruction, phase correction and fat–water separation described above.

### 3.4. Flow-independent angiography application

Balanced SSFP sequences produce good angiographic contrast. In the foot, where (at 1.5 T) it is not always possible to achieve an adequate shim for balanced SSFP images, dual-acquisition SSFP has a useful application. We scanned the feet of five healthy volunteers using a  $70^\circ$  flip angle,  $TR=2TE=4.6$  ms, a  $384\times128\times128$  matrix and a  $38\times12\times12\text{-cm}$  FOV for 1-mm isotropic resolution.

The acquisition was repeated for both RF phase cycle schemes, as with the abovementioned scans. Complex images were reconstructed for both acquisitions, and the phase correction and fat–water separation were performed on both the source images and the complex sum. MIP images were calculated from the water image for both source images and the complex sum image.

## 4. Results

Results from phantom and in vivo validation, as well as the high-field and magnetization-prepared applications, are shown in Figs. 4–8.

### 4.1. Phantom validation

The magnitude and phase images from the phantom validation of this technique are shown in Fig. 4. The top two rows show the magnitude [(A) and (C)] and phase [(B) and (D)] of the individual scans. No effort was made to correct the timing mismatch between readout gradient and acquisition, so there is a small linear phase along the bottle in addition to the phase transitions shown in Fig. 1. Fat is seen at the top of the images; water, at the bottom. Note that a phase change of  $\pi$  occurred both at the fat–water boundary and across the signal nulls due to resonance frequency changes. Also note that changes from black to white are simply phase wraps of  $2\pi$  and are not significant. The next rows show the magnitude and phase of the complex sum of the individual images before [(E) and (F)] and after [(G) and (H)] phase correction was applied. Finally, the separated fat [(I)] and water [(J)] images are shown at the left and the right.

There is a slight ripple in the magnitude images from the complex sum [13,14]. However, the phase was completely flat, resulting in the correct separation of fat and water over most of the phantom. Near the right end of the bottle, however, the algorithm failed because the spatially varying resonance frequency shift was too rapid.

### 4.2. In vivo validation

Figs. 5 and 6 show images of the knee and lower leg of a healthy volunteer with and without a constant gradient of 0.1 mT/m, respectively. Fig. 5 shows that the final image magnitude has some ripple due to significant resonant frequency variations. However, the dark bands present in the two source images have been removed. The magnitude variations are much less noticeable in Fig. 6, where the field

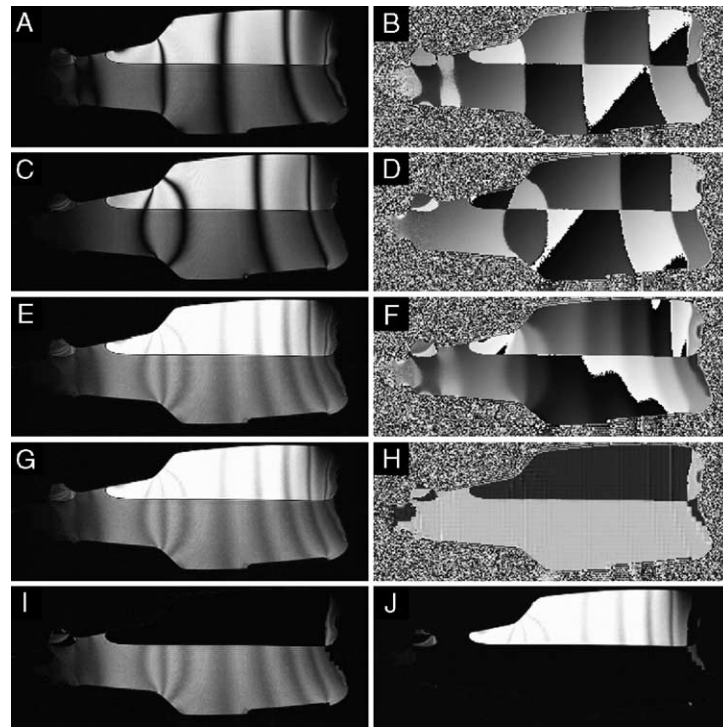


Fig. 4. Magnitude and phase images of a fat–water bottle phantom. Magnitude [Panels (A) and (C)] and phase [Panels (B) and (D)] images for  $\Delta\phi=0$  and  $\Delta\phi=\pi$ , respectively. Magnitude [Panels (E) and (G)] and phase [Panels (F) and (H)] of the complex sum image before and after phase correction, respectively. Magnitude images of water [Panel (I)] and fat [Panel (J)] following voxel separation. The phase correction removes the slowly-varying phase but preserves the sign difference between fat and water signals so that fat and water images can be separated. The high susceptibility shift at the right end of the bottle causes the algorithm to fail.

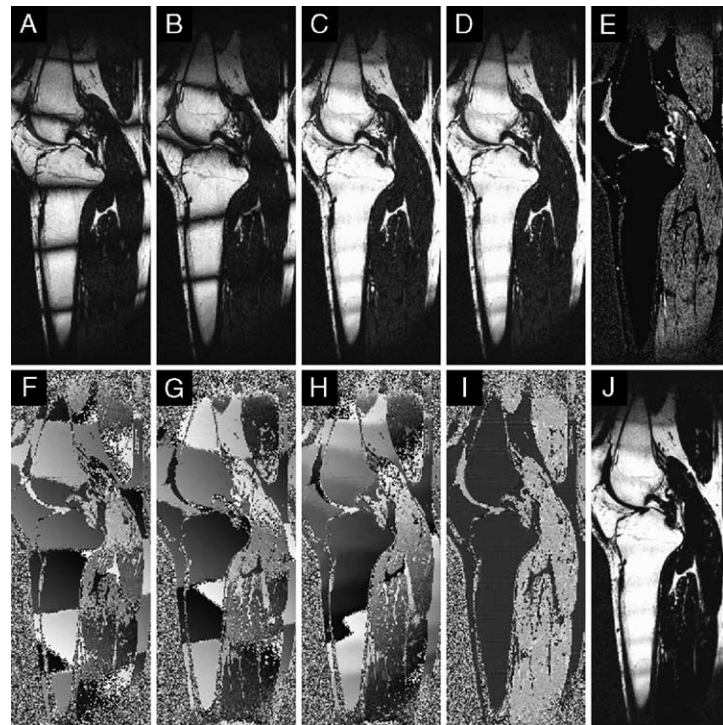


Fig. 5. Magnitude and phase images of the knee and lower leg of a healthy volunteer when a constant gradient of 0.1 mT/m was applied in the superior/inferior direction. Magnitude [Panels (A) and (B)] and phase [Panels (F) and (G)] images for  $\Delta\phi=0$  and  $\Delta\phi=\pi$ , respectively. Magnitude [Panels (C) and (D)] and phase [Panels (H) and (I)] of complex sum image before and after phase correction, respectively. Magnitude images of water [Panel (E)] and fat [Panel (J)] following voxel separation. (The water image is displayed with a window level that is three times lower than that of other magnitude images.)



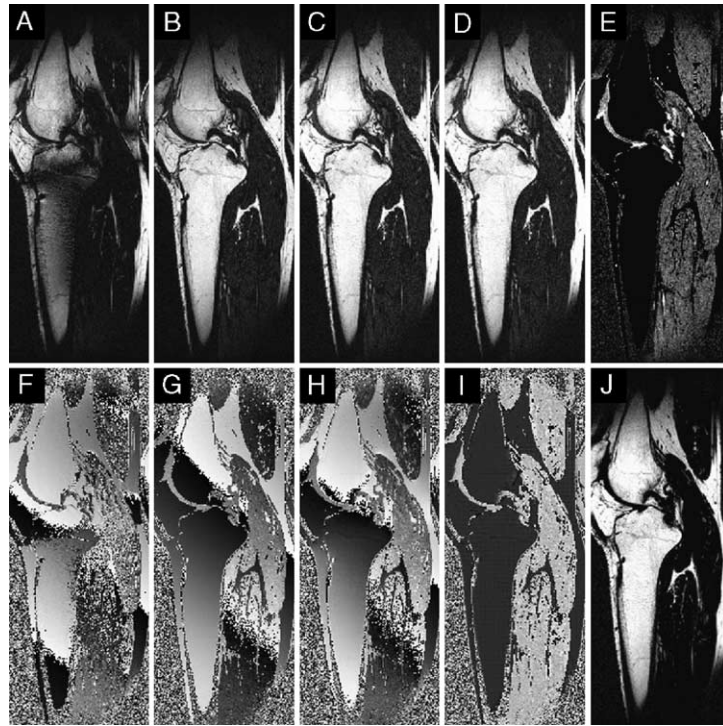


Fig. 6. Magnitude and phase images of the knee and lower leg of a healthy volunteer with no constant gradient applied. Magnitude [Panels (A) and (B)] and phase [Panels (F) and (G)] images for  $\Delta\phi=0$  and  $\Delta\phi=\pi$ , respectively. Magnitude [Panels (C) and (D)] and phase [Panels (H) and (I)] of complex sum image before and after phase correction, respectively. Magnitude images of water [Panel (E)] and fat [Panel (J)] following voxel separation. (Again, the water image is displayed with a window level that is three times lower than that of other magnitude images.)

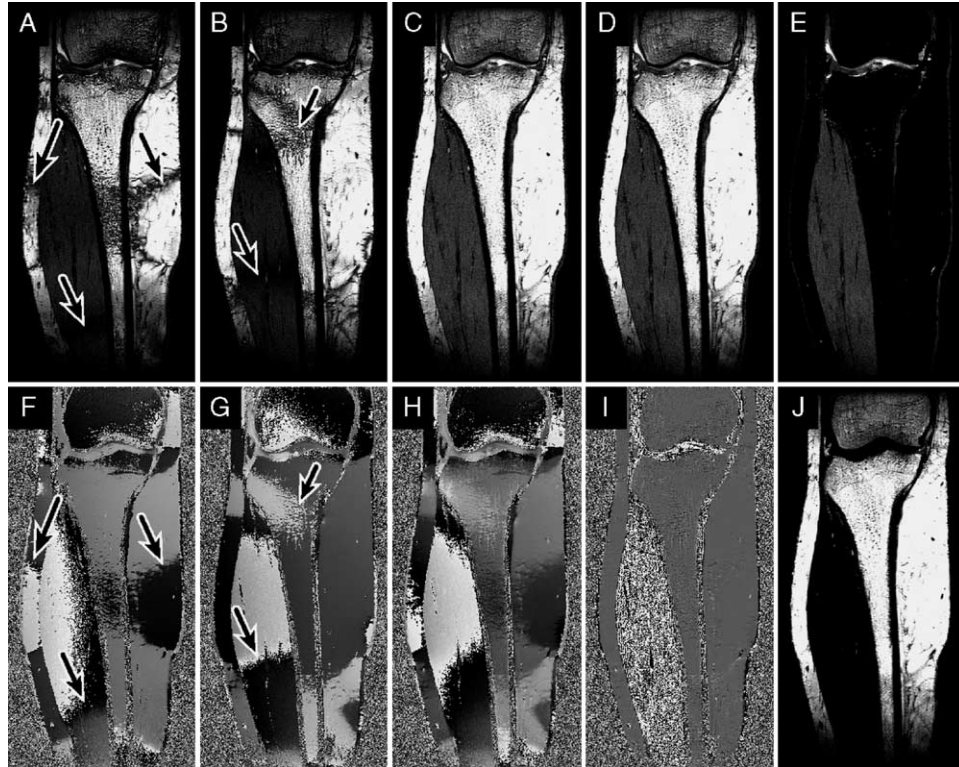


Fig. 7. Example of fat–water separation in the knee and lower leg of a healthy volunteer using two acquisitions with  $TR=2TE=11.9$  ms at 3.0 T. Magnitude [Panels (A) and (B)] and phase [Panels (F) and (G)] images for  $\Delta\phi=0$  and  $\Delta\phi=\pi$ , respectively. Magnitude [Panels (C) and (D)] and phase [Panels (H) and (I)] of complex sum image before and after phase correction, respectively. Magnitude images of water [Panel (E)] and fat [Panel (J)] following voxel separation. Arrows show dark bands corresponding to low-signal regions in the source images that are completely removed in the final images.

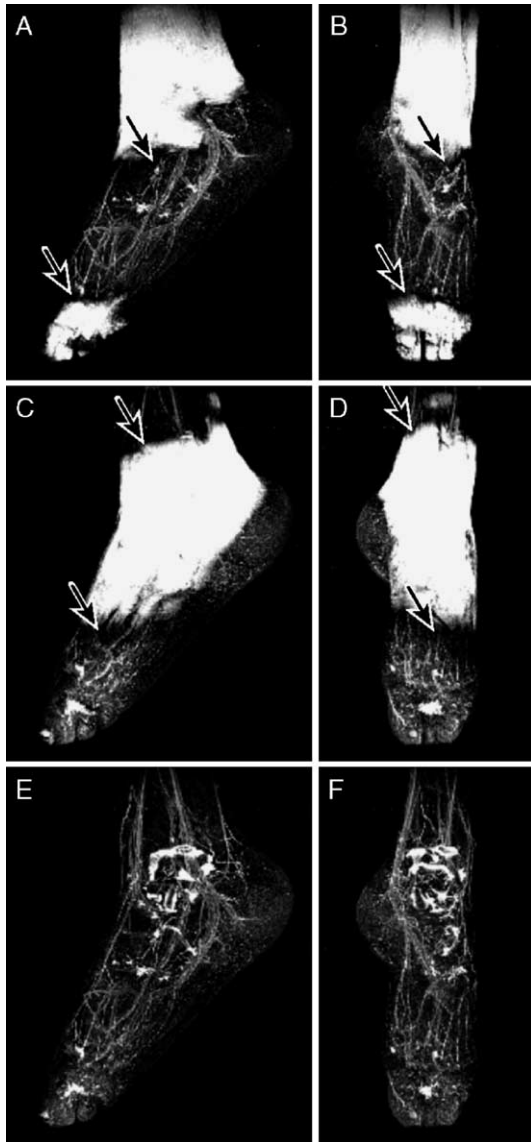


Fig. 8. MIP sagittal [Panels (A), (C) and (E)] and coronal [Panels (B), (D) and (F)] images from a balanced SSFP image of the foot of a healthy volunteer. In the individual acquisitions [Panels (A)–(D)], single-acquisition phase-sensitive SSFP [24] misplaced fat and water when the image contained signal nulls (arrows), with the result that subcutaneous fat obscures visualization of the vasculature. However, the MIPs from the dual-acquisition phase-sensitive separation [Panels (E) and (F)] clearly show the vasculature in the water image. The bright synovial fluid could be suppressed by combining this technique with magnetization preparation schemes [33,40].

variation is that of a typical scan. There is no noticeable difference in the image phase after phase correction [Fig. 6(I) vs. Fig. 5(I)], indicating that the fat–water separation is not affected by a reasonably large field variation along the knee.

#### 4.3. Images at 3.0 T

Fig. 7 shows the source images, reconstruction and separated images in the lower leg of a volunteer when the acquisition was at 3.0 T, using  $TR=11.9$  ms. With these parameters, the fat and water peaks are five SSFP passbands

apart. Significant dark band artifacts are clear in the source images, as shown by the arrows in Fig. 7[(A), (B), (F) and (G)]. These dark bands are removed by the phase correction, and the final images again show good separation of fat and water with very minimal brightness variation due to the SSFP signal profile.

#### 4.4. Angiographic images

MIPs of the magnetization-prepared water images acquired using a  $\Delta\phi$  of 0 and  $\pi$  are shown in Fig. 8. In the foot, where susceptibility variations are large, single-acquisition phase-sensitive separation resulted in misplacement of fat and water voxels in the source images [Fig. 8(A), (B), (C) and (D)]. However, when the phase correction and separation were applied to the complex sum of two acquisitions, the fat and water were properly separated and the vasculature was clearly shown [Fig. 8(E) and (F)].

### 5. Discussion

We have shown and validated a dual-acquisition phase-sensitive fat–water separation technique that significantly decreases the sensitivity of balanced SSFP to resonance offsets as compared with previously presented techniques. As with phase-sensitive SSFP [24], this technique exploits the signal sign change between fat and water in different SSFP signal bands. By selecting  $TR$  equal to the reciprocal of the frequency difference between fat and water, voxels can be separated based on the signal difference. In the dual-acquisition technique, the same sign change is present in both acquisitions, but an additional phase results when the signals are combined by complex addition. By using a phase-correction technique, the slowly varying phase can be removed while preserving the sign change between fat and water voxels.

In the remainder of this section, we discuss some of the implementation and parameter choices, as well as the sensitivity of the technique to practical issues such as field variations and partial-volume effects.

#### 5.1. Multiple center frequency or phase cycling

The Theory section here assumes that the two (or more) source images used to generate an improved signal profile are acquired by phase cycling (i.e., changing only the phase increment of the excitation and acquisition). Although this is the same as changing the center frequency of the scan by  $\Delta f = \Delta\phi / (2\pi TR)$  theoretically [28], it is much better to increment the RF and acquisition phase in practice for several reasons as discussed here. First, the signal phase alternates between  $\Delta\phi/2 + \pi/2$  and  $\Delta\phi/2 - \pi/2$  so that no rephasing is required during the image combination. Second, if the excitation is selective, shifting the center frequency will shift the slice. However, this is a subtle effect in 3D imaging and is not usually noticeable. Third, the

different center frequency means that the shift along the readout direction is different in different scans. Again, this could be corrected with care in reconstruction. Fourth, in real imaging sequences, the phase reference of RF and acquisition pulses often precedes the waveform by some amount. This results in an additional phase that differs with center frequency. Again, this can be corrected with careful consideration. All of these effects show that it is advantageous to modulate the phase of the pulses rather than to change the scan center frequency.

### 5.2. Selection of $TR$ and $TE$

The selection of  $TR$  and  $TE$  is important for this method. First, we have chosen  $TR$  such that the band spacing in frequency is equal to the chemical shift frequency between fat and water. For this method, this is also the frequency difference that will *always* result in a phase shift of exactly  $180^\circ$  between fat and water. Second, we have assumed that  $TE=TR/2$ . Selection of a different  $TE$  will result in an additional linear phase  $\phi=2\pi\Delta f(TE-TR/2)$ . It is possible to select a different combination of  $TE$  and  $TR$  to still achieve approximately a  $180^\circ$  separation between fat and water. In fact, simply choosing  $TE$  so that  $210\text{ Hz}=(2n-1)/(2TE)$ , where  $n=1,2,3,\dots$ , will work well in most cases (at 1.5 T). We have shown that it is also possible to implement this method such that the fat–water chemical shift frequency difference is  $(2n+1)/TR$ , for any integer  $n$ . As  $n$  increases leads to a more rapidly changing phase, which does reduce robustness.

### 5.3. Cell size

Selection of the cell size is a tradeoff between sensitivity to noise and sensitivity to resonant frequency shifts. A larger cell size provides good noise immunity. However, if the resonant frequency shift within the cell is significant, then the phase fit is poor, leading to poor robustness. Thus, a small cell size allows for rapid frequency changes, provided that the SNR is reasonable.

### 5.4. Dependence on $T_1$ , $T_2$ and flip angle

The balanced SSFP signal is dependent on offset frequency,  $T_1$ ,  $T_2$ ,  $TR$  and flip angle. At  $TE=TR/2$ , the signal for a particular species can be viewed as a Fourier series,  $S(f) = \sum_{n=1}^{\infty} A_n \cos[(2n-1)\pi f TR]$ , as described in Reference [32]. The amplitude of  $A_n$  for higher harmonics increases as  $T_2/T_1$  increases or as the flip angle decreases. The separation method we have shown would work best when  $A_n=0$  for  $n>1$  (i.e., the signal has only one harmonic). As the amplitude of higher harmonics increases, the transitions become more difficult for the phase correction to track and the method will be less reliable. This suggests using reasonably large flip angles.

### 5.5. Sensitivity to $B_0$ and $B_1$

The balanced SSFP signal is given in numerous references, such as References [6] and [7]. Interestingly,

the signal phase is completely independent of the flip angle. For single-acquisition phase-sensitive SSFP [24], this means that the separation is insensitive to  $B_1$ . However, for dual-acquisition phase-sensitive SSFP,  $B_1$  variations can cause a change in the signal shape (as with flip angle, described above), which makes separation more difficult.

The motivation for the dual-acquisition (rather than single-acquisition) technique is to reduce  $B_0$  sensitivity. Although the signal is still sensitive to  $B_0$ , the sensitivity is reduced to that of previous dual-acquisition SSFP techniques [7,11–14]. The technique is not limited by the size of  $B_0$  variations but rather by the rate of such changes. Thus, it can withstand significantly greater  $B_0$  variations than all other balanced SSFP fat-suppressed techniques.

### 5.6. Partial-volume sensitivity

Like phase-sensitive SSFP, dual-acquisition phase-sensitive SSFP images the fat–water difference [24]. When fat and water occupy a single voxel, their signals compete, with the voxel appearing as the dominant material. This effect is true of most balanced SSFP sequences, unless the fat and water signals are placed in the same signal passband by the use of a very short  $TR$ . This partial-volume effect can be a significant limitation compared with Dixon SSFP [22] and is an important consideration in selecting the spatial resolution and the appropriateness of this technique for particular imaging applications.

### 5.7. Multiple acquisitions

In this article, we have shown a dual-acquisition SSFP technique. As described previously [11,13,14], the use of more acquisitions can smooth the magnitude response. For phase-sensitive detection, the acquisitions can be simply added, provided that phase cycling is used as described above. As the number of acquisitions is increased, the phase of the combined acquisitions becomes more linear, which is very desirable. The SNR efficiency, however, decreases as the higher harmonics of the signal profile are suppressed. Ultimately, the SNR efficiency and contrast approach those of gradient-spoiled imaging techniques.

### 5.8. Magnetization-prepared SSFP

The balanced SSFP sequence can be preceded by a magnetization preparation stage, such as inversion recovery [33,34],  $T_2$  preparation [35] and myocardial tagging [36,37]. If a ramp-like full- $TR$  preparation [38,39] is used between the preparation and imaging stages, the sign difference in signal at the middle of adjacent bands is quickly achieved. Our initial tests have shown that single-acquisition or dual-acquisition phase-sensitive tissue separation is fully compatible with magnetization-prepared sequences [40].

## 6. Conclusion

Dual-acquisition phase-sensitive SSFP is a method that applies a phase correction to the combination of two



standard balanced SSFP acquisitions, which then enables simple separation of fat and water based on the sign of the signal. The strength of this method is that it addresses the sensitivity of balanced SSFP to off-resonance effects and, in addition, allows separation of fat and water. Although there is some efficiency loss in the dual-acquisition SSFP technique, it exhibits comparable or better SNR or CNR efficiency when compared with gradient echo and spoiled gradient echo fat-suppressed options. Overall, the technique is somewhat insensitive to static field inhomogeneity and susceptibility and RF field variations. Dual-acquisition phase-sensitive SSFP has been validated for imaging of the periphery at both 1.5 and 3.0 T and may allow significantly improved arterial–venous contrast for peripheral angiography.

### Acknowledgments

This work was supported by the NIH (NIH-1R01EB002524, NIH-01HL075803 and NIH-1R01HL074332) and GE Healthcare Technologies.

### Appendix A

We provide the mathematical details of the block-regional phase correction used to remove the slowly varying phase while preserving phase shifts from the chemical shift between fat and water. Fig. 2 is a 2D illustration of these steps.

Step 1 consists of simply dividing the image into blocks. We will assign a complex value of  $c_{x,y,z}$  to each block, where  $x$ ,  $y$  and  $z$  are the coordinates of the block. For simplicity, we also define the phase of a block as  $\phi_{x,y,z} = \angle c_{x,y,z}$ .

In Step 2, the complex block values are determined. The phase of a block is found by the following formula:

$$\phi_{x,y,z} = \frac{1}{2} \arctan2D \left( \sum_{k=1}^N 2a_k b_k, \sum_{k=1}^N a_k^2 - \sum_{k=1}^N b_k^2 \right) \quad (1)$$

where  $a_k$  and  $b_k$  are the real and imaginary components of each voxel within the block and  $k$  represents the  $k$ th voxel of the  $N$  voxels within the block.  $\phi_{x,y,z}$  is found for all blocks, in any order. It can be shown that Eq. (1) gives the angle of a line through the origin that minimizes the sum of the squares of the distances from a set of points to the line. (In Fig. 2, these best-fit lines are shown as black dashed lines and the orthogonal distances are shown as dotted lines.)

It is important to use a 2D (or four-quadrant)  $\arctan2D$  function in Eq. (1), which returns an angle between  $-\pi$  and  $\pi$  rather than between  $-\pi/2$  and  $\pi/2$ . The  $180^\circ$  ambiguity of using a 1D  $\arctan$  function means that  $\phi$  could be the angle of the line that maximizes the sum of squared distances.

$|c_{x,y,z}|$  is simply the sum of absolute values of the dot products of each pixel in the block with a unit vector along

the best-fit line, the length of the gray arrows in Fig. 2. Mathematically,

$$|c_{x,y,z}| = \sum_{k=1}^N a_k \cos \phi_{x,y,z} - b_k \sin \phi_{x,y,z} \quad (2)$$

In Step 3, the blocks are ordered by the distance from the starting block and processed in order so as to keep the phase consistent (Order A–B–C–D in Fig. 2). For this processing step, the product  $p = c_{x,y,z}^* c_n$  is calculated, where  $c_n$  is the complex sum of  $c_{x,y,z}$  for all blocks that are closer to the starting block and  $c_{x,y,z}^*$  denotes the complex conjugate of  $c_{x,y,z}$ . If the real part of  $p$  is negative, then the value of  $c_{x,y,z}$  is negated. Note that all of these calculations are insensitive to discontinuities of  $2\pi$ . (Gray arrows in Fig. 2 show the corrected magnitude and direction of  $c_{x,y,z}$  for each of the four cells.)

In Step 4, all voxels within the block at  $(x,y,z)$  are simply multiplied by  $e^{-i\phi_{x,y,z}}$ .

Our phase-correction software is available in both Matlab and C at <http://www-mrsl.stanford.edu/~brian/psssf/>.

As a final note, Eq. (1) is derived as the solution to the line through the origin that minimizes the sum of squares of orthogonal distances to the complex scatter. More simply,  $\phi$  is half the angle of the sum of the squares of each complex scatter point, as described in Reference [29].

### References

- [1] Carr HY. Steady-state free precession in nuclear magnetic resonance. *Phys Rev* 1958;112:1693–701.
- [2] Oppelt A, Graumann R, Barfuss H, Fischer H, Hartl W, Shajor W. FISP—a new fast MRI sequence. *Electromedica* 1986;54:15–8.
- [3] Duerk JL, Lewin JS, Wendt M, Petersilge C. Remember true FISP? A high SNR near 1-second imaging method for  $T_2$ -like contrast in interventional MRI at .2 T. *J Magn Reson Imaging* 1998;8:203–8.
- [4] Freeman R, Hill HDW. Phase and intensity anomalies in Fourier transform NMR. *J Magn Reson* 1971;4:366–83.
- [5] Zhang W, Kramer D. A single point quadrature Dixon method for water fat separated MRI using phase-cycled SSFP. *Proceedings of the 45th ENC, Asilomar*; 2004. p. 6.
- [6] Buxton RB, Fisel CR, Chien D, Brady TJ. Signal intensity in fast NMR imaging with short repetition times. *J Magn Reson* 1989; 83:576–85.
- [7] Zur Y, Stokar S, Bendel P. An analysis of fast imaging sequences with steady-state transverse magnetization refocusing. *Magn Reson Med* 1988;6:175–93.
- [8] Scheffler K, Lehnhardt S. Principles and applications of balanced SSFP techniques. *Eur Radiol* 2003;13:2409–18.
- [9] Heid O. 3D MR angiography with non-selective excitation. *Proceedings of the 8th Annual Meeting of ISMRM, Denver*; 2000. p. 1784.
- [10] Lu A, Barger AV, Grist TM, Block WF. Improved spectral selectivity and reduced susceptibility in SSFP using a near zero TE undersampled three-dimensional PR sequence. *J Magn Reson Imaging* 2004; 19:117–23.
- [11] Haacke EM, Wielopolski PA, Tkach JA, Modic MT. Steady-state free precession imaging in the presence of motion: application for improved visualization of the cerebrospinal fluid. *Radiology* 1990; 175:545–52.

- [12] Kurucay S, Schmalbrock P, Chakeres DW, Keller PJ. A segment-interleaved motion-compensated acquisition in the steady state (Simcast) technique for high resolution imaging of the inner ear. *J Magn Reson Imaging* 1997;7:1060–8.
- [13] Vasanawala SS, Pauly JM, Nishimura DG. Linear combination steady-state free precession MRI. *Magn Reson Med* 2000;43:82–90.
- [14] Bangerter NK, Hargreaves BA, Vasanawala SS, Pauly JM, Gold GE, Nishimura DG. Analysis of multiple-acquisition SSFP. *Magn Reson Med* 2004;51:1038–47.
- [15] Deshpande VS, Shea SM, Laub G, Simonetti OP, Finn JP, Li D. 3D magnetization-prepared true-FISP: a new technique for imaging coronary arteries. *Magn Reson Med* 2001;46:494–502.
- [16] Scheffler K, Heid O, Hennig J. Magnetization preparation during the steady-state: fat-saturated 3D true FISP. *Magn Reson Med* 2001;45:1075–80.
- [17] Hargreaves BA, Vasanawala SS, Pauly JM, Nishimura DG. Characterization and reduction of the transient response in steady-state MR imaging. *Magn Reson Med* 2001;46:149–58.
- [18] Vasanawala SS, Pauly JM, Nishimura DG. Fluctuating equilibrium MRI. *Magn Reson Med* 1999;42:876–83.
- [19] Hardy CJ, Dixon WT. Steady-state free precession imaging with inherent fat suppression. *Proceedings of the 10th Annual Meeting of ISMRM, Honolulu*; 2002. p. 473.
- [20] Overall WR, Nishimura DG, Hu BS. Steady-state sequence synthesis and its application to efficient fat-suppressed imaging. *Magn Reson Med* 2003;50:550–9.
- [21] Leupold J, Scheffler K, Hennig J. Fast fat saturation for balanced SSFP imaging at low flip angles using alternating TR. *Proceedings of the 12th Annual Meeting of ISMRM, Kyoto*; 2004. p. 266.
- [22] Reeder SB, Alley MT, Pelc NJ, Gold GE. Rapid MR imaging of articular cartilage with steady-state free precession and multipoint fat–water separation. *AJR Am J Roentgenol* 2003;180:357–62.
- [23] Huang TY, Chung HW, Wang FN, Ko CW, Chen CY. Fat and water separation in balanced steady-state free precession using the Dixon method. *Magn Reson Med* 2004;51:243–7.
- [24] Hargreaves BA, Vasanawala SS, Nayak KS, Hu BS, Nishimura DG. Fat-suppressed steady-state free precession imaging using phase detection. *Magn Reson Med* 2003;50:210–3.
- [25] Lu A, Brodsky E, Grist TM, Block WF. Rapid fat-suppressed isotropic steady-state free precession imaging using true 3D multiple-half-echo projection reconstruction. *Magn Reson Med* 2005;53:692–9.
- [26] Yu H, Reeder SB, Markl M, Pelc NJ. Single acquisition water fat separation for SSFP cardiac CINE imaging: feasibility study. *Proceedings of the 12th Annual Meeting of ISMRM, Kyoto*; 2004. p. 263.
- [27] Gurney P, Hargreaves B, Nishimura D. Improved fat-suppressed SSFP imaging using 3DPR. *Proceedings of the 12th Annual Meeting of ISMRM, Kyoto*; 2004. p. 2133.
- [28] Hinshaw WS. Image formation by nuclear magnetic resonance: the sensitive-point method. *J Appl Phys* 1976;47:3709–21.
- [29] Ma J. Breath-hold water and fat imaging using a dual-echo two-point Dixon technique with an efficient and robust phase-correction algorithm. *Magn Reson Med* 2004;52:415–9.
- [30] Moriguchi H, Lewin JS, Duerk JL. Fast spiral two-point Dixon technique using block regional off-resonance correction. *Magn Reson Med* 2004;52:1342–50.
- [31] Dharmakumar R, Hong J, Brittain JH, Plewes DB, Wright GA. Oxygen-sensitive contrast in blood for steady-state free precession imaging. *Magn Reson Med* 2005;53:574–83.
- [32] Kim DJ, Cho ZH. Analysis of the higher-order echoes in SSFP. *Magn Reson Med* 1991;19:20–30.
- [33] Deimling M, Heid O. Magnetization prepared true FISP imaging. *Proceedings of the 2nd Annual Meeting of SMR, San Francisco*; 1994. p. 495.
- [34] Scheffler K, Hennig J.  $T_1$  quantification with inversion recovery TrueFISP. *Magn Reson Med* 2001;45:720–3.
- [35] Shea SM, Deshpande VS, Chung YC, Li D. Three-dimensional true-FISP imaging of the coronary arteries: improved contrast with  $T_2$ -preparation. *J Magn Reson Imaging* 2002;15:597–602.
- [36] Zwanenburg JJ, Kuijter JP, Marcus JT, Heethaar RM. Steady-state free precession with myocardial tagging: CSPAMM in a single breathhold. *Magn Reson Med* 2003;49:722–30.
- [37] Herzka DA, Guttman MA, McVeigh ER. Myocardial tagging with SSFP. *Magn Reson Med* 2003;49:329–40.
- [38] Nishimura DG, Vasanawala SS. Analysis and reduction of the transient response in SSFP imaging. *Proceedings of the 8th Annual Meeting of ISMRM, Denver*; 2000. p. 301.
- [39] Le Roux P. Simplified model and stabilization of SSFP sequences. *J Magn Reson* 2003;163:23–37.
- [40] Bangerter NK, Hargreaves BA, Brittain JH, Hu B, Vasanawala SS, Nishimura DG. 3D fluid-suppressed  $T_2$ -prep flow-independent angiography using balanced SSFP. *Proceedings of the 12th Annual Meeting of ISMRM, Kyoto*; 2004. p. 11.